CRYSTAL GROWTH & DESIGN

Article

pubs.acs.org/crystal

Synthesis, Crystal Structure, and Physical Properties of Two Polymorphs of $CsGaSe_2$, and High-Temperature X-ray Diffraction Study of the Phase Transition Kinetics

Daniel Friedrich,[†] Marc Schlosser,[†] and Arno Pfitzner*[,†]

[†]Institut für Anorganische Chemie, Universität Regensburg, Universitätsstraße 31, 93040 Regensburg, Germany

Supporting Information

ABSTRACT: The light gray selenogallate $CsGaSe_2$-*mC*64 was obtained by reaction of stoichiometric amounts of CsN_3, GaSe, and Se at elevated temperatures. Its crystal structure was determined by single-crystal X-ray diffraction. The compound crystallizes in the monoclinic space group *C*2/*c* (No. 15) with a = 11.043(2) Å, b = 11.015(4) Å, c = 16.810(2) Å, β = 99.49(1) °, V = 2016.7(8) Å^3, and Z = 16 (powder data, ambient temperature). Its crystal structure features anionic layers $^2_\infty[Ga_4Se_8^{4-}]$ consisting of corner-sharing Ga_4Se_{10} supertetrahedra. The compound undergoes a first-order phase transition at temperatures of 610 ± 10 °C. The high-temperature phase $CsGaSe_2$-*mC*16 also crystallizes in the monoclinic space group *C*2/*c* (No. 15) with a = 7.651(3) Å, b = 12.552(4) Å, c = 6.170(3) Å, β = 113.62(4)°, V = 542.9(5) Å^3, and Z = 4 (powder data, ambient temperature). The crystal structure of the high-temperature phase consists of SiS_2 analogous chains $^1_\infty[GaSe_2^-]$. *In situ* high-temperature X-ray diffraction experiments were performed to study this phase transition. The crystallization kinetics of the phase transitions were studied using Johnson−Mehl−Avrami−Kolmogorov (JMAK) theory for isothermal crystallization processes. The activation energy of the phase transition was determined using the Arrhenius equation. Furthermore, the compound was studied by vibrational and diffuse reflectance spectroscopy.

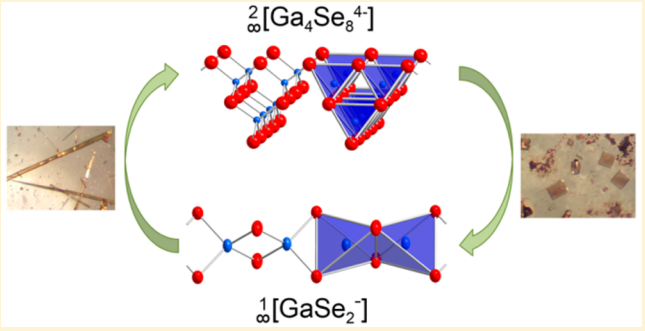

INTRODUCTION

Group 13 chalcogenometallates containing alkali metal cations crystallize in a large variety of different structures.[1] Multinary chalcogenometallates are important materials for technical applications due to their semiconducting properties.[2,3] Most of the crystal structures of the known phases in the ternary systems of alkali metal, triel, and chalcogen consist of linked MQ_4-tetrahedra (M = Al, Ga, In; Q = S, Se, Te) embedded in a cationic surrounding of alkali metal ions. The resulting anionic substructures composed of these connected tetrahedra range from discrete tetrahedra to more complex one-, two-, and three-dimensional networks. All previously known compounds in the system cesium, gallium, and selenium contain infinite one-dimensional selenogallate anions. The phases $Cs_6Ga_2Se_6$,[4] $Cs_8Ga_4Se_{10}$,[4] and $Cs_{10}Ga_6Se_{14}$[4] feature edge-sharing dimeric, tetrameric, and hexameric selenogallate units. $Cs_2Ga_2Se_5$[5] and $CsGaSe_3$[6] contain polychalcogenide units Se_2^{2-}, and consist of infinite anionic chains $^1_\infty[Ga_2Se_3(Se_2)^{2-}]$ and $^1_\infty[Ga_2Se_2(Se_2)_2^{2-}]$, respectively. Prior studies by Deiseroth et al.[7] revealed that two polymorphs of $CsGaSe_2$ might exist; however, no crystal structures (besides comparisons of powder diffraction patterns) or details of the phase transition were reported. Recently we reported on some details of the crystal structures and the phase transition temperatures of $CsGaSe_2$,[8] which we will now discuss in more detail. Furthermore, the progress of the phase transition is observed using *in situ* high-temperature X-ray diffraction. The kinetics of the isothermal phase transitions are studied using Johnson−Mehl−Avrami−Kolmogorov (JMAK) theory,[9] yielding information on the crystallization behavior and activation energy.

RESULTS AND DISCUSSION

Single-Crystal Structure Determination. $CsGaSe_2$ forms air and moisture sensitive colorless crystals. The crystal structures were determined from single-crystal X-ray diffraction data collected at 123 K. Both solids crystallize in the monoclinic space group *C*2/*c* (No. 15) with a = 11.0011(6) Å, b = 11.0007(6) Å, c = 16.7390(8) Å, β = 99.465(4)°, V = 1998.2(2) Å^3, and Z = 16 for $CsGaSe_2$-*mC*64, and a = 7.6458(3) Å, b = 12.5337(5) Å, c = 6.1634(3) Å, β = 113.716(4)°, V = 540.76(4) Å^3, and Z = 4 for $CsGaSe_2$-*mC*16. The change of Z by a factor of 4 comes along with a change of the unit cell volume by almost a factor of 4; that is, the structural changes are accompanied by a change of the density.

The crystal structures were solved by charge flipping methods using SUPERFLIP,[10] implemented in Jana2006,[11] and refined to R_1 = 0.0547 and wR_2 = 0.0668 for $CsGaSe_2$-

Received: April 7, 2016
Revised: May 19, 2016
Published: May 24, 2016

DOI: 10.1021/acs.cgd.6b00532
Cryst. Growth Des. 2016, 16, 3983−3992

Table 1. Crystallographic Data for $CsGaSe_2$-*mC*64 and $CsGaSe_2$-*mC*16

	$CsGaSe_2$-*mC*64	$CsGaSe_2$-*mC*16
Formula weight/g·mol^{-1}		360.553
Color, shape, crystal size/mm^3	Colorless plate, 0.12 × 0.04 × 0.02	Colorless rod, 0.29 × 0.04 × 0.02
Crystal system, space group		Monoclinic, *C*2/*c* (No. 15)
Lattice constants from single crystals		
a/Å	11.0011(6)	7.6458(3)
b/Å	11.0007(6)	12.5337(5)
c/Å	16.7390(8)	6.1634(3)
β/Å	99.465(4)	113.716(4)
Volume *V*/Å^3	1998.2(2)	540.76(4)
Number of formula units *Z*	16	4
Calculated density ρ_{calc}/g·cm^{-3}	4.794	4.427
Temperature *T*/°C		−150(1)
Diffractometer		Rigaku Supernova
Wavelength *λ*/Å		0.71073
Absorption coeff. *μ*(Mo K*α*)/mm^{-1}	27.069	25.002
θ range of data collection/deg	3.39−29.1	3.25−29.03
Index range	$-14 \le h \le 14$	$-10 \le h \le 10$
	$-14 \le k \le 14$	$-16 \le k \le 17$
	$-22 \le l \le 22$	$-8 \le l \le 8$
Absorption correction		Analytical, CrysAlisPro[14]
No. of reflections collected	23138	10383
Independent reflections	2597	1021
R_{int}	0.0449	0.0466
Completeness to *θ* = 25°	99.9%	99.9%
Structure solution		Charge flipping, Superflip[10]
Structure refinement		Jana2006[11]
No. of refined parameters	75	22
No. of constraints	0	0
Extinction coefficient G_{iso}	−	0.0008(1)
Twin law	−1 0 0, 0 −1 0, 1/2 0 1	1 0 1, 0 −1 0, 0 0 −1
Twin fraction	41.6%	13.8%
GooF	1.30	1.17
R_1, wR_2 [$I > 3\sigma(I)$]	0.0237, 0.0481	0.0205, 0.0439
R_1, wR_2 [all data]	0.0547, 0.0668	0.0271, 0.0484
Largest diff. peak and hole/e·Å^{-3}	1.13, −1.35	0.43, −0.50

[a]Further details on the crystal structure investigations may be obtained from the Fachinformationszentrum Karlsruhe, 76344 Eggenstein-Leopoldshafen, Germany (fax: (+49)7247-808-666; E-mail: crysdata@fiz-karlsruhe.de), on quoting the depository number CSD-431161 ($CsGaSe_2$-*mC*64) and CSD-431160 ($CsGaSe_2$-*mC*16). They are also deposited under the numbers CCDC 1474649 ($CsGaSe_2$-*mC*16) and CCDC 1474650 ($CsGaSe_2$-*mC*64).

*mC*64 and $R_1 = 0.0271$ and $wR_2 = 0.0484$ for $CsGaSe_2$-*mC*16 by full-matrix least-squares methods using Jana2006.[11] Both polymorphs exhibited twinning. The twin matrices were analyzed using TwinRotMat of the PLATON software package.[12] Details on the final crystallographic data and details of the structure solution and refinement are listed in Tables1−3. Anisotropic displacement parameters, interatomic distances, and angles can be found in the Supporting Information (Table S1−S4).

The low-temperature phase $CsGaSe_2$-*mC*64 crystallizes isotypic to many related compounds MTQ_2 (*M* = Na, K, Rb, Cs, Tl; *T* = Al, Ga, In; *Q* = S, Se, Te) in the $TlGaSe_2$ structure type.[13] The crystal structure features anionic layers $^2_\infty[Ga_4Se_8^{4-}]$, consisting of four corner-sharing Ga_4Se_{10} supertetrahedra, stacked along [001] and separated by Cs atoms (Figure 1). Both independent trivalent gallium sites have a slightly distorted tetrahedral coordination formed by four Se atoms. The interatomic distances range from *d*(Ga−Se) = 2.384(1) Å to *d*(Ga−Se) = 2.444(1) Å with a mean bond length of $\bar{d}$(Ga−Se) = 2.413(1) Å. The angles ∠(Se−Ga−Se) range from 105.85(4)° to 114.08(3)°.

Table 2. Atomic Coordinates and Equivalent Isotropic Displacement Parameters U_{eq} (in Å^2) for $CsGaSe_2$-*mC*64

Atom	Wyck.	*x*	*y*	*z*	U_{eq}[a]
Cs1	8*f*	0.2867(1)	0.0622(1)	0.3970(1)	0.0099(1)
Cs2	8*f*	0.4626(1)	0.3126(1)	0.1013(1)	0.0088(1)
Ga1	8*f*	0.1040(1)	0.1890(1)	0.1714(1)	0.0050(2)
Ga2	8*f*	0.1432(1)	0.4361(1)	0.3287(1)	0.0048(2)
Se1	8*f*	0.0421(1)	0.3124(1)	0.4186(1)	0.0080(2)
Se2	8*f*	0.2082(1)	0.0626(1)	0.0836(1)	0.0061(1)
Se3	8*f*	0.2577(1)	0.3117(1)	0.2502(1)	0.0063(2)
Se4	4*e*	0	0.0542(1)	1/4	0.0055(3)
Se5	4*e*	0	0.5694(1)	1/4	0.0067(3)

[a]U_{eq} is defined as one-third of the trace of the orthogonalized U_{ij} tensor.

Both distances and angles are in good agreement with comparable compounds.[4−8,15−17] The bond lengths differ slightly from the sum of the ionic radii,[18] *d*(Ga^{3+}−Se^{2-}) ∼

DOI: 10.1021/acs.cgd.6b00532
Cryst. Growth Des. 2016, 16, 3983−3992

Table 3. Atomic Coordinates and Equivalent Isotropic Displacement Parameters U_{eq} (in Å^2) for $CsGaSe_2$-*mC16*

Atom	Wyck.	*x*	*y*	*z*	U_{eq}[a]
Cs	4*e*	0	0.14166(2)	1/4	0.0346(1)
Ga	4*e*	0	0.50303(4)	1/4	0.0194(2)
Se	8*f*	0.18562(4)	0.39467(3)	0.09752(6)	0.0248(1)

[a] U_{eq} is defined as one-third of the trace of the orthogonalized U_{ij} tensor.

2.5 Å. Four $GaSe_4$ tetrahedra share common corners to build Ga_4Se_{10} supertetrahedra. These units are linked by common Se2 corners forming anionic layers $^2_\infty[Ga_4Se_8^{4-}]$ parallel to (110). The layers are penetrated by cesium atoms. The two independent cesium sites are 6+2-fold coordinated by selenium, resulting in bicapped trigonal prisms (Figure 1). These prisms are connected by common edges (Se3, Se4; Se3, Se5) and the capping atoms (Se1, Se2). The interatomic distances in the trigonal prisms range from d(Cs−Se) = 3.5913(1) Å to d(Cs−Se) = 3.675(1) Å with a mean bond length of $\bar{d}$(Cs−Se) = 3.636(1) Å, whereas the distances to the capping atoms are larger with d(Cs−Se2) = 3.900(1) to d(Cs−Se1) = 3.907(1) Å. The distances in the trigonal prisms are almost identical to the sum of the ionic radii[18] $d(Cs^+-Se^{2-}) \sim 3.7$ Å. The interatomic distances of the cesium atoms in one layer are below d(Cs−Cs) < 5 Å, whereas the distances between adjacent layers are in the range d(Cs−Cs) = 5.482(1)−5.526(1) Å. The 8-fold interconnected cesium atoms form an irregular topological network.

The high-temperature phase $CsGaSe_2$-*mC16* crystallizes isotypic to $CsGaS_2$ in the $KFeS_2$ structure type.[19] The anionic structure consists of infinite SiS_2 analogous chains $^1_\infty[GaSe_2^-]$ separated by a cationic cesium substructure. The gallium atoms are 4-fold coordinated by selenium atoms, resulting in slightly distorted $GaSe_4$ tetrahedra. The interatomic distances are d(Ga−Se) = 2.4084(4) Å and d(Ga−Se) = 2.4114(5) Å. The angles ∠(Se−Ga−Se) range from 100.48(1)° to 115.67(2)°. Both distances and angles are in good agreement with comparable compounds.[4−8,15−17] The bond lengths are slightly smaller than the sum of the ionic radii[18] $d(Ga^{3+}-Se^{2-}) \sim 2.5$ Å. Each $GaSe_4$ tetrahedron is connected to two adjacent tetrahedra by common edges, resulting in an infinite anionic chain $^1_\infty[GaSe_2^-]$ running along [001]. The cesium atoms are 8-fold "coordinated" by selenium, resulting in irregular polyhedra with interatomic distances ranging from d(Cs−Se) = 3.7452(5) to d(Cs−Se) = 3.8359(4) Å. These Cs−Se distances in the trigonal prisms coincide with the sum of the ionic radii[18] $d(Cs^+-Se^{2-}) \sim 3.7$ Å. The Cs cations form a cubic diamond analogous topology of 4-fold connected Cs atoms with distances of d(Cs−Cs) = 4.6915(5) Å and 4.7018(4) Å. The angles ∠(Cs−Cs−Cs), ranging from 81.904(7)° to 130.762(4)°, however, differ significantly from an ideal tetrahedral environment.

Thermal Analysis. A differential thermal analysis (DTA) was performed to determine the temperature region of the phase transition from $CsGaSe_2$-*mC64* to $CsGaSe_2$-*mC16* (Figure 2). The measurement (heating/cooling rate 10 °C/min, 2 cycles) revealed a reversible phase transition to the high-temperature modification starting at 610 °C and a transition back to the low-temperature phase starting at 530 °C. The second cycle shows a differing intensity for the signal of the back-transition to the low-temperature phase. The integrated peak intensity in both cycles is almost identical. The difference in the absolute intensity and onset temperature might result from an incomplete transformation and residual nuclei of both polymorphs, or from some sintering of the sample at high temperatures.

High-Temperature X-ray Diffraction and Kinetic Study. Following the determination of an approximate temperature region, we decided to further study this phase

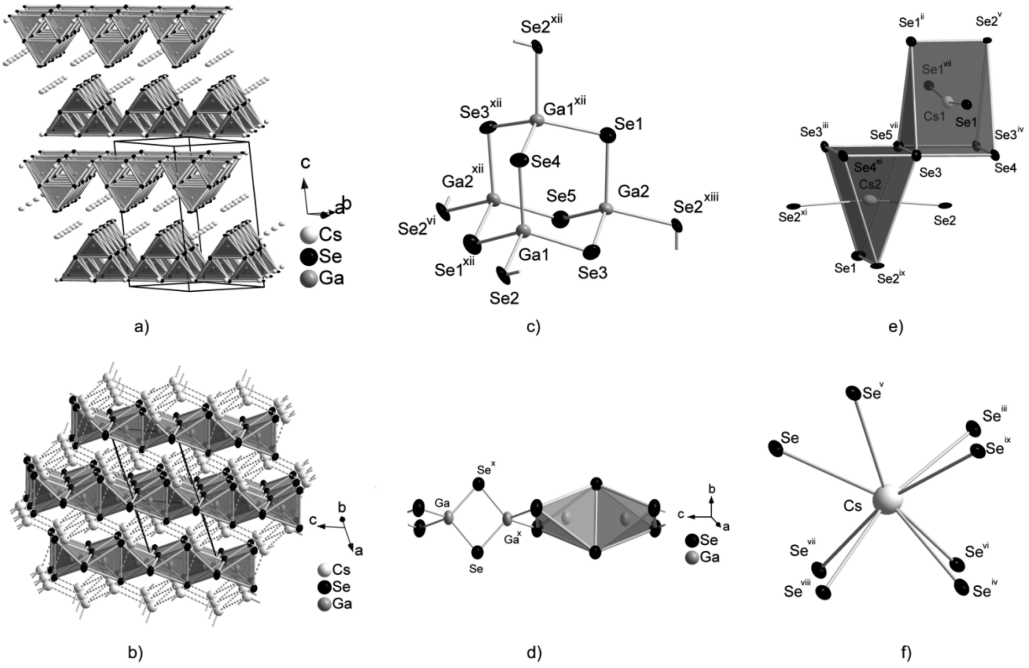

Figure 1. Comparison of the crystal structures of both $CsGaSe_2$ polymorphs, showing: (a) the stacking of anionic layers in *mC64*; (b) arrangement of the anionic chains in *mC16* (dashed lines indicate the diamond-like Cs substructure); (c) supertetrahedral unit Ga_4Se_{10} in *mC64*; (d) SiS_2 analogous anionic chain in *mC16*; (e) coordination polyhedra of the Cs sites in *mC64*. (f) coordination of the Cs site in *mC16*.

DOI: 10.1021/acs.cgd.6b00532
Cryst. Growth Des. 2016, 16, 3983−3992

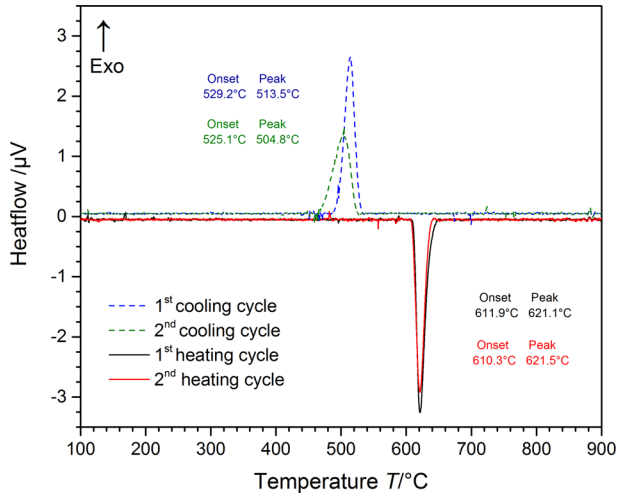

Figure 2. Differential thermal analysis (DTA) plot of the phase transition of $CsGaSe_2$ (the baseline was manually subtracted). The four heating and cooling cycles (heating/cooling rate 10 °C/min) reveal a reversible phase transition.

transition using high-temperature X-ray diffraction methods to gain insight into the crystallization behavior and phase transition kinetics of the compound.

Experimental Setup. The measurements were performed on a STOE Stadi P diffractometer (monochromatized Mo Kα1 radiation, λ = 0.70930 Å) equipped with a Dectris Mythen 1K detector and a high-temperature capillary furnace. As there is a significant influence of grain sizes on the reaction kinetics, all samples were sieved prior to the experiments using analytical sieves. The smallest fraction with a grain size distribution of 0.02−0.04 mm was used for all experiments. The air sensitive samples were loaded into flame-sealed quartz glass capillaries (diameter 0.3 mm). For all experiments, a 2θ range of 4.55−23.420° (exposure time: 180 s per pattern) containing the most significant reflections of both polymorphs was measured. All diffraction patterns were analyzed using the STOE $WinX^{POW}$ software package.[20] Reflection profiles were fitted using a pseudo-Voigt shape. Usage of an internal standard (Al_2O_3) for the determination of the phase fractions resulted in falsification of the data due to extremely accelerated phase transitions, even for the smallest amounts of impurities (<2% w/w). The phase fractions α were therefore determined using a linear regression of the integrated intensities of the strongest reflections for both polymorphs ($CsGaSe_2$-*mC*64: −224, 13.6° 2θ; $CsGaSe_2$-*mC*16: −221, 12.7° 2θ). Falsification of the obtained intensities due to texture effects of the plate- and rod-shaped crystallites was not observed. Figure 3 shows a typical plot of the time-resolved transformation from the low-temperature to the high-temperature phase.

Nonisothermal Analysis. The region of the phase transition previously investigated by thermal analysis was also studied using high-temperature X-ray powder diffraction. The sample was heated from room temperature to 600 °C, and diffraction patterns were collected until the sample reached 650 °C (step: 1 °C, holding time: 5 min, heating rate 1 °C/min). Afterward, the sample was annealed at 700 °C for 60 min to ensure a complete phase transition. Finally, the compound was cooled to 600 °C and measured until 520 °C (step: 1 °C, holding time: 5 min, heating rate 1 °C/min). The phase fractions of both polymorphs plotted against the measurement temperature show a sigmoidal shape, with the phase transition from

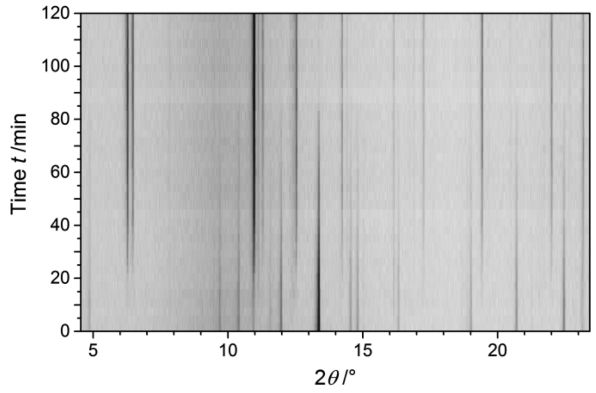

Figure 3. Top view of a time-resolved 3D plot of the phase transition from $CsGaSe_2$-*mC*64 (bottom) to -*mC*16 (top) (T = 620 °C).

$CsGaSe_2$-*mC*64 to $CsGaSe_2$-*mC*16 beginning at ∼625 °C and the transition back starting at ∼545 °C, as seen in Figure 4. These values slightly differ from the thermal analysis, but can easily be explained by the different heating and cooling rates during the measurements.

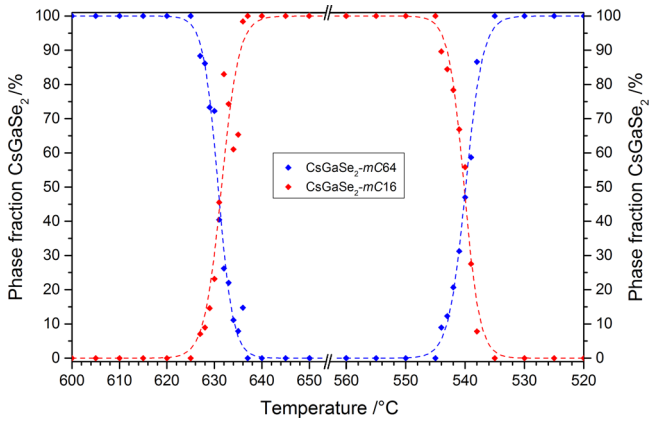

Figure 4. Progression of the phase fractions of the *mC*64 (blue) and *mC*16 (red) polymorphs during heating and cooling of the sample (heating/cooling rate 1 °C/min).

Isothermal Kinetic Analysis. Kinetic analyses of solid-state crystallization are usually performed by fitting the obtained experimental data of the extent of the phase formation α as a function of time to a theoretical expression. Table 4 shows some kinetic expressions previously applied in the literature.[21] For the determination of the isothermal kinetic parameters, a modified JMAK equation (eq 1) with the reaction exponent n and the kinetic rate constant K was used.[9] This equation is widely known for its application in the study of crystallization kinetics of various compounds.[22−24] Equation 2 is the linearized form of the JMAK equation. The Avrami exponent n is determined by plotting $\ln[-\ln[(1-\alpha)^{-1}]$ against $\ln(t)$, the so-called Sharp−Hancock plot.[25] The slope of this linear plot yields the Avrami exponent n for each step of the crystallization. This exponent is related to the morphology of the crystallites and the nucleation and growth processes during crystallization. More than one linear part in this plot is a sign that the crystallization does not proceed by one uniform mechanism. The rate constant K is determined by the intercept of the y-axis. All kinetic parameters were determined after subtraction of the individual induction times t_0, as the value of n is very dependent

DOI: 10.1021/acs.cgd.6b00532
Cryst. Growth Des. 2016, 16, 3983−3992

Table 4. Common Functions of Rate Equations Used for the Comparison of Solid-State Reactions[21] in the Form of a Constant Factor $c(t/t_{0.5})$ ($t_{0.5}$ = time necessary for 50% crystallization)

Growth model	Rate equation $f(\alpha) = c(t/t_{0.5})$	n
Diffusion controlled		
D1(α)	$\alpha^2 = 0.25(t/t_{0.5})$	0.62
D2(α)	$(1-\alpha)\ln(1-\alpha) + \alpha = 0.1534(t/t_{0.5})$	0.57
D3(α) [Jander]	$[1-(1-\alpha)^{1/3}]^2 = 0.0426(t/t_{0.5})$	0.54
D4(α) [Ginstling–Brounshtein]	$1 - 2\alpha/3 - (1-\alpha)^{2/3} = 0.0367(t/t_{0.5})$	0.57
Phase-boundary controlled		
R2(α)	$[1-(1-\alpha)^{1/2}] = 0.2929(t/t_{0.5})$	1.04
R3(α)	$[1-(1-\alpha)^{1/3}] = 0.2063(t/t_{0.5})$	1.08
First order		
F1(α)	$[-\ln(1-\alpha)] = 0.6931(t/t_{0.5})$	1
Nucleation & Growth [JMAK]		
A2(α)	$[-\ln(1-\alpha)]^{1/2} = 0.8326(t/t_{0.5})$	2
A3(α)	$[-\ln(1-\alpha)]^{1/3} = 0.8850(t/t_{0.5})$	3
A4(α)	$[-\ln(1-\alpha)]^{1/4} = 0.9125(t/t_{0.5})$	4

on the chosen t_0. The incubation time t_0 herein is defined as the time until a reflection of the growing phase is observed in the diffraction pattern.

$$\alpha(t) = 1 - \exp[-(Kt)^n] \quad (1)$$

$$\ln[-\ln(1-\alpha)^{-1}] = n\ln(t) + n\ln(K) \quad (2)$$

The phase transition from $CsGaSe_2$-*mC*64 to the high-temperature phase *mC*16 was studied in the temperature region from 620 to 630 °C with an irradiation time of 180 s for 620 °C and 60 s for 625 and 630 °C (per pattern) to take the fast phase transitions into account. Other temperatures resulted in a transition which was either too fast or too slow for a rational study. The Avrami exponents, reaction rates, and characteristic times for all experiments are listed in Table 5. The plot of the time $t-t_0$ against the extent of the phase transition α for all investigated temperatures (Figure 5a, b) shows a decreasing time for a complete phase transition at higher temperatures. The incubation times t_0 also drop from 12 min at 620 °C to about 1 min at 625 and 630 °C. This trend is in accordance with an increased crystal growth rate at higher temperatures. The Avrami exponents n in the range of 0.9(3) to 1.6(1) suggest a one-dimensional growth of the crystallites with a decreasing nucleation rate as dominant growth mechanism, which is in accordance with the rod-shaped crystallites of $CsGaSe_2$-*mC*16. In the initial stage of the phase transition at 620 °C (α < 40%), a drop of n to 0.81(9) is observed, indicating a different growth mechanism. To determine this mechanism, a plot of $t/t_{0.5}$ against α is used and compared with curves for the different mechanisms listed in Table 4. This plot (Figure 6) shows a good agreement for the initial transition with the R2 and R3 curves, both models of a phase-boundary controlled growth. After this stage, the plot follows JMAK kinetics. A similar behavior is also present to a small degree in the plot for 625 °C. Due to the relatively fast transformation, only two data points could be obtained for α < 40%, thus complicating the determination of the exact mechanism. This change leads to the conclusion that this phase transition starts with a preferred nucleation at grain boundaries. At temperatures higher than 625 °C, the growth is dominated by JMAK growth kinetics.

Taking the reversibility of the phase transition into account, we additionally decided to perform a similar study for the phase transition from $CsGaSe_2$-*mC*16 to $CsGaSe_2$-*mC*64. The experiments were performed in the temperature region from 560 to 540 °C with an irradiation time of 180 s (per pattern). Although reproducible data could be obtained for all experiments, the possible influence of supercooling and related phenomena cannot be neglected completely. Furthermore, the samples were heated to 700 °C for 1 h prior to the measurement. This treatment ensured a pure sample of the high-temperature polymorph, as the transition back to the low-temperature phase already progressed in the time interval necessary to heat up to the desired temperature. Sintering of the samples during this time was not observed. The Avrami exponents, reaction rates, and characteristic times for all experiments are listed in Table 5. The plot of the time $t-t_0$ against the extent of the phase transition α interestingly shows an increasing time for a complete phase transition at higher temperatures for all investigated temperatures (Figure 5c, d). The incubation time t_0 also significantly increases at higher temperatures.

Although this fact may at first sight be counterintuitive, we suggest the following explanation. Even though the crystal growth rate increases with increasing temperature, a higher

Table 5. Reaction Rate Constants K and Avrami Exponents n of the Phase Transition Kinetics Analysis of $CsGaSe_2$ Obtained by Using the Avrami Equation and Sharp–Hancock Plot for Different Temperatures T

Transition	T/°C	t_0/min	$t_{0.5}$/min	Mechanism	Avrami exponent n	Rate constant K/min^{-1}
*mC*64 → *mC*16	620, α < 40	12(3)	42	R2/R3	0.81(9)	$1.6(7) \times 10^{-2}$
	620, α > 40			A2	1.47(4)	$1.9(2) \times 10^{-2}$
	625	1(1)	3	A2	1.6(1)	$3.0(4) \times 10^{-1}$
	630[a]	1(1)[a]	1.5[a]	A2[a]	0.9(3)[a]	$0.4(1) \times 10^{0}$[a]
*mC*16 → *mC*64	540	6(3)	8.5	A3	2.7(3)	$1.1(2) \times 10^{-1}$
	545	18(3)	21	A3	2.55(5)	$4.1(3) \times 10^{-2}$
	550, α < 40	27(3)	55	R2/R3	1.45(9)	$1.4(3) \times 10^{-2}$
	550, α > 40			A3	2.70(9)	$1.6(2) \times 10^{-2}$
	555, α < 15	246(3)	180	R2/R3	0.40(4)	$0.9(8) \times 10^{-2}$
	555, α > 15			A3	2.74(4)	$4.8(4) \times 10^{-6}$
	560	84(3)	210	R2/R3	1.20(1)	$3.6(2) \times 10^{-3}$

[a]Results based on only 3 data points during the transition.

DOI: 10.1021/acs.cgd.6b00532
Cryst. Growth Des. 2016, 16, 3983–3992

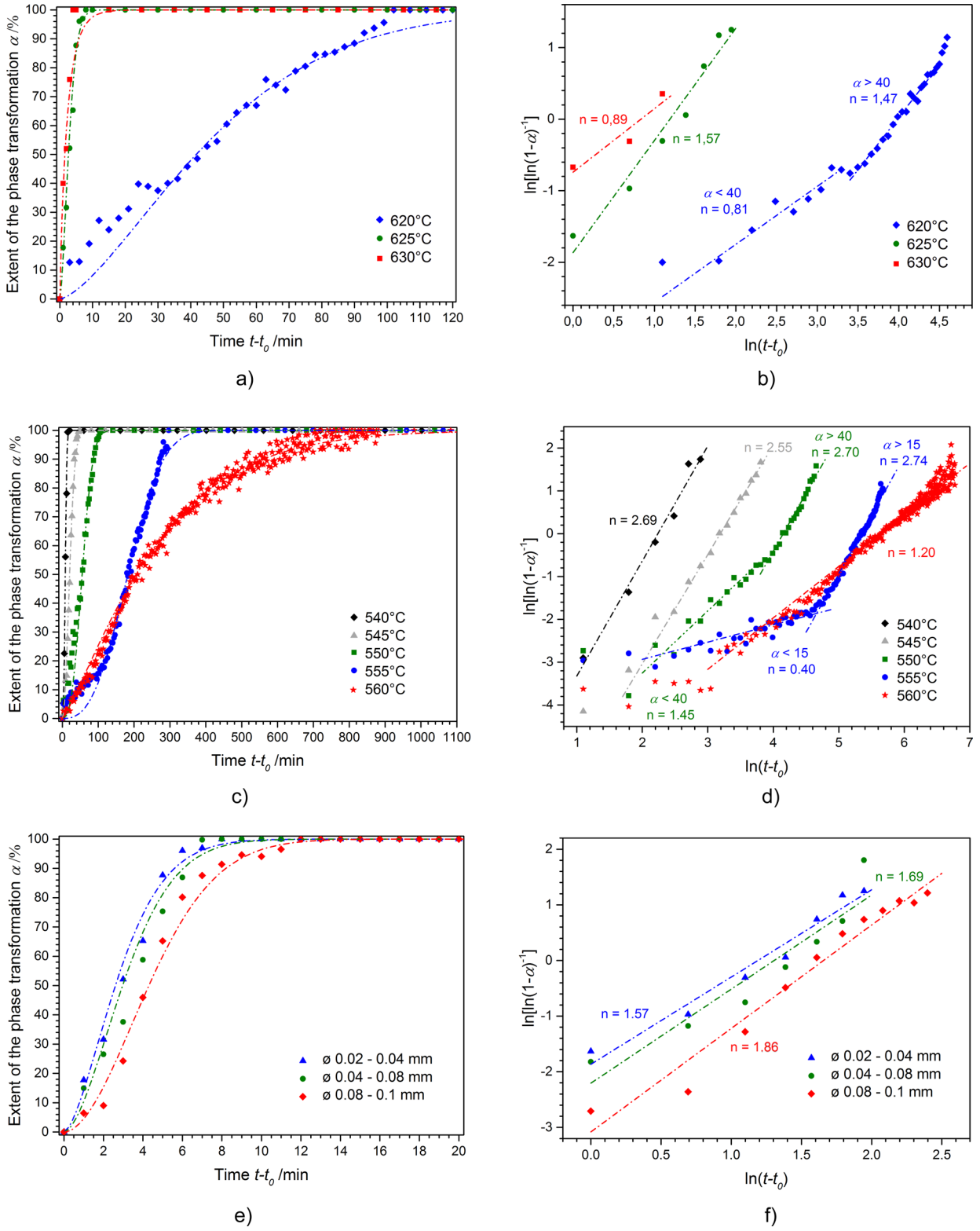

Figure 5. (a) Plots of the progression of the phase transitions from $CsGaSe_2$-*mC*64 to $CsGaSe_2$-*mC*16 and (c) $CsGaSe_2$-*mC*16 to $CsGaSe_2$-*mC*64 and (e) the different grain sizes investigated at 625 °C (Dashed lines indicate a fit based on the JMAK equation using the experimentally determined parameters *n* and *K* for the dominating growth mechanism). The Sharp−Hancock plots to determine *n* are also shown for (b) the transition from $CsGaSe_2$-*mC*64 to $CsGaSe_2$-*mC*16 and (d) $CsGaSe_2$-*mC*16 to $CsGaSe_2$-*mC*64 and (f) the different grain sizes investigated at 625 °C (Dashed lines indicate linear fits with the slope *n* and *k* the intercept at the *y*-axis).

degree of supercooling in the sample leads to an increased amount of crystal nuclei present. The increased amount of nuclei significantly decreases the time necessary for a quantitative transformation. This fact is supported by a trend of larger half widths of the reflections of the growing phase during the initial stages of the crystallization for decreasing

DOI: 10.1021/acs.cgd.6b00532
Cryst. Growth Des. 2016, 16, 3983−3992

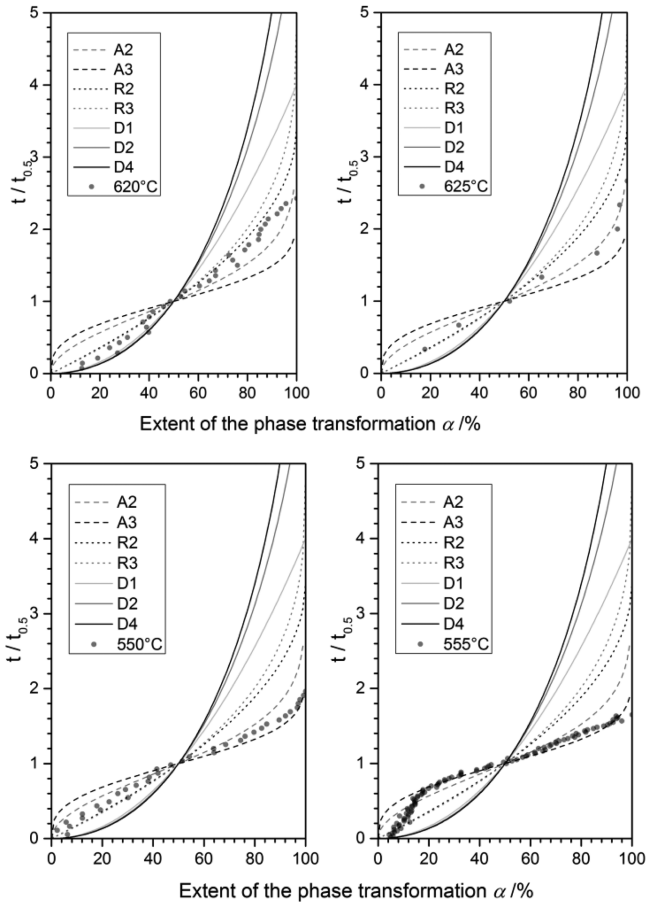

Figure 6. Plot of α against $t/t_{0.5}$ for the transitions at different temperatures compared with curves for the common kinetic models in Table 4.

temperatures. In the course of the phase transition, the half widths significantly decrease until they reach a constant value (Figure S4). Fitting of the obtained diffraction patterns using a LeBail fit (based on a fundamental parameter approach) in Jana2006[11] also revealed a slight trend of increasing crystallite sizes and a slight decrease in crystal strain in the course of each transition. The Avrami exponents n in the range 2.55(5) to 2.74(4) suggest a two-dimensional growth with a decreasing nucleation rate, which is in good agreement with the plate-shaped crystallites of $CsGaSe_2$-*mC*64. The Avrami exponents in the range 540−555 °C during the growth period are almost identical within the margin of standard deviations, indicating no significant change of the dominating growth mechanism. A closer investigation of the Sharp−Hancock plot revealed a second linear part during the initial stages of the phase transition at 550 °C (α < 40%) and 555 °C (α < 15%). For 560 °C a significantly lower value of n is also observed. These significantly lower values of n indicate a different growth mechanism. To determine this mechanism, a plot of $t/t_{0.5}$ against α is used and compared with curves for the different mechanisms listed in Table 4. This plot (Figure 6) shows a good agreement for the initial transition with the R2 and R3 curves, both models of a phase-boundary controlled growth. After this stage, the plots for 550 and 555 °C once again follow JMAK kinetics. The curve for 560 °C continues to follow the curve of R3. The nucleation step in phase-boundary controlled reactions occurs almost instantly, covering the surface of the powder with a layer of the product phase. After this, the interface grows at a constant rate.[26] Therefore, combined with our experimental results, crystallization during the phase transition from $CsGaSe_2$-*mC*16 to $CsGaSe_2$-*mC*64 can be explained with the following behavior. If there is a significant degree of supercooling, the initial crystallization will be dominated by a phase-boundary controlled growth on the crystallite surface. At higher temperatures, the possibility of the formation of new nuclei in the sample according to the JMAK theory is possible. As soon as these new nuclei are large enough, the crystallization will be dominated by nucleation and growth according to the JMAK theory.

Influence of Grain Sizes. The preparation of samples with a uniform crystallite shape and a small grain size distribution seems to be the most important factor to obtain reproducible results. To study the influence of the grain size on the phase transition from $CsGaSe_2$-*mC*64 to -*mC*16, samples of different grain size in the range 0.02 mm to 0.1 mm were prepared and measured at 625 °C (Figure 5e, 5f). The diffraction patterns of the different samples showed decreasing FWHMs with increasing grain sizes, confirming different grain sizes. The resulting reaction times, Avrami exponents, and rate constants are listed in Table 6. A slight trend of increasing incubation times t_0 and transformation time $t-t_0$ can be observed upon increasing the grain size. The Avrami exponent n slightly increases from 1.6(1) to 1.9(1) but stays almost within the range of the e.s.d.s, suggesting no significant change in the growth mechanism for the examined grain sizes. The slower transformation rates can be explained by a decreasing contact of the crystallites in the powder, and a subsequent decrease of possible nucleation sites. A comparison of a plot of $t/t_{0.5}$ against α compared with curves for the different mechanisms listed in Table 4 shows no change in the growth mechanism. A slightly smaller contribution of phase-boundary growth at the initial stage of the transition for the sample with a grain size 0.08−0.1 mm (Figure S3) can be observed.

Summary. The phase transition from the low-temperature phase $CsGaSe_2$-*mC*64 to the high-temperature phase $CsGaSe_2$-*mC*16 proceeds with a one-dimensional growth mechanism (A2) according to the JMAK theory. At higher temperatures, less time for a complete transformation is necessary. The Avrami exponents are in the range from 0.9(3) to 1.6(1). This behavior is in accordance with the rod-shaped crystallites. The initial stage of crystallization is dominated by a phase-boundary controlled mechanism (R2/R3). The influence of this change in mechanism decreases with increasing temperature. Increasing the crystallite size leads to a slightly increased transition time with no significant change in the growth mechanism;

Table 6. Influence of Different Grain Sizes on the Phase Transition of $CsGaSe_2$-*mC*64 at 625 °C

T/°C	Grain size/mm	t_0/min	$t_{0.5}$/min	Mechanism	Avrami exponent n	Rate constant K/min^{-1}
625	0.02−0.04	1(1)	3	A2	1.6(1)	$3.0(4) \times 10^{-1}$
625	0.04−0.08	4(1)	3.5	A2	1.7(3)	$2.7(6) \times 10^{-1}$
625	0.08−0.1	4(1)	4.5	A2	1.9(1)	$1.9(2) \times 10^{-1}$

DOI: 10.1021/acs.cgd.6b00532
Cryst. Growth Des. 2016, 16, 3983−3992

albeit, an increase of n up to 1.9(1) is observed. The phase transition back to the low-temperature phase $CsGaSe_2$-*mC*64 proceeds with a two-dimensional growth mechanism (A3), which fits well with the plate-shaped crystallites. The initial stages of crystallization at 550 and 555 °C are also dominated by a phase-boundary controlled process (R2/R3) with a decreasing influence at higher temperatures. At 560 °C the whole transition proceeds by this phase-boundary controlled mechanism. At higher temperatures, an increase in the time necessary for a complete transition was observed. We propose that these observations are due to the influence of supercooling.

Activation Energies. The activation energy of the phase transition was calculated using the Arrhenius equation and plotting T^{-1} against the logarithm of the obtained reaction rate constants K for all measurements (Figure 7). The value

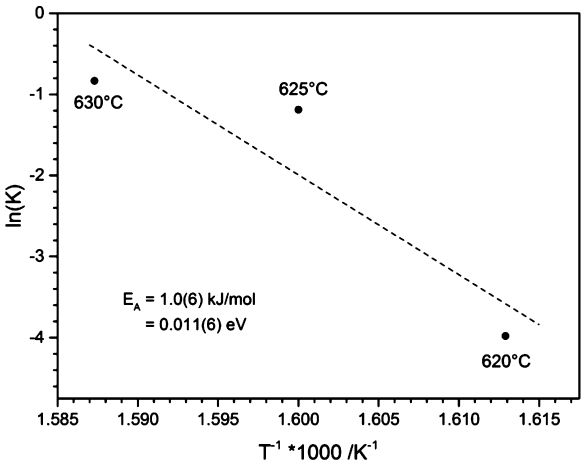

Figure 7. Arrhenius plot used for the determination of the activation energies for the phase transitions *mC*64 → *mC*16 (The dashed line indicates a linear fit used to determine the activation energy).

obtained for the transition to the high-temperature phase $CsGaSe_2$-*mC*16 is E_A = 1.0(6) kJ/mol. This value represents the effective activation energy for both nucleation and growth.[27]

Vibrational Spectroscopy. The measured Raman spectra of both polymorphs of $CsGaSe_2$ are shown in Figure 8. Vibrational bands below 105 cm^{-1} can be attributed to lattice

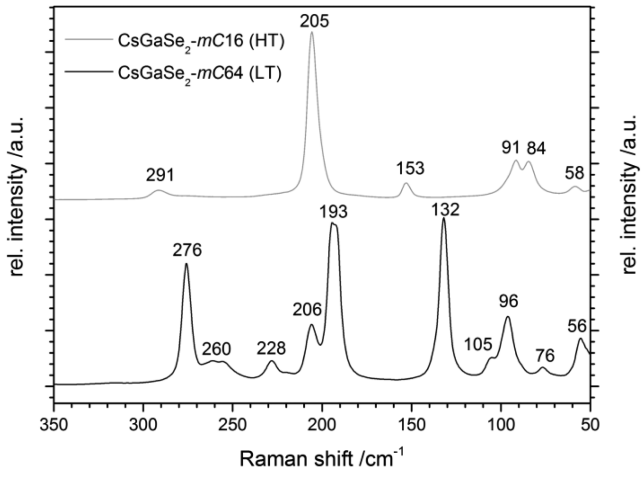

Figure 8. Raman spectra of both $CsGaSe_2$ polymorphs (bottom: *mC*64, top: *mC*16).

vibrations, whereas the peaks at 132, 153, and 193 cm^{-1} are tentatively assigned to Cs−Se stretching vibrations.[5,6] All higher Raman shifts can be attributed to Ga−Se stretching modes.[5,6]

UV/Vis-Spectroscopy. The optical band gaps of the $CsGaSe_2$ polymorphs were determined by UV/vis diffuse reflectance spectroscopy (Figure 9). The absorption data were

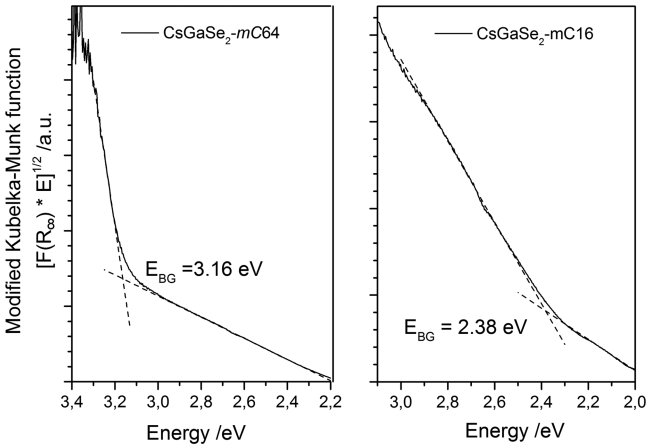

Figure 9. Diffuse reflectance spectrum of both $CsGaSe_2$ polymorphs (left: *mC*64, right: *mC*16). The band gaps were determined by extrapolation of the linear part of the modified Kubelka−Munk function onto the baseline, as indicated by the dashed lines.

calculated using a modified Kubelka−Munk function.[28] Extrapolation of the linear part onto the baseline resulted in the wide band gaps of 3.16 eV for $CsGaSe_2$-*mC*64 and 2.38 eV for $CsGaSe_2$-*mC*16. The observed band gaps for both compounds are in good agreement with the white and yellow colors of both powdered polymorphs, respectively. The band gap of $CsGaSe_2$-*mC*16 follows the trend of an increasing band gap with a decreasing polyselenide content observed in the system $Cs_2[Ga_2Se_{4-x}(Se_2)_x]$,[5,6] as previously reported.[5]

Electronic Structure Calculations. Several attempts have been made to calculate the electronic band structures of both polymorphs of $CsGaSe_2$ from relativistic DFT calculations. The application of several different functionals always resulted in well matching band gaps for the high-temperature phase $CsGaSe_2$-*mC*16 (exp: 2.38 eV, calc: ∼ 2.5 eV). Significant discrepancies between experimental and calculated band gaps for the low-temperature phase $CsGaSe_2$-*mC*64 were observed (exp: 3.16 eV, calc: ∼ 2.0 eV). Similar calculations for $KAlQ_2$ (Q = Se, Te) were reported by Benmakhlouf et al.,[29] but they cannot be compared with experimental data yet. These calculations are the subject of a forthcoming project.[30]

■ CONCLUSION

In this work, we present the crystal structures of two polymorphs of $CsGaSe_2$. This compound undergoes a reversible polymorphic phase transition, starting at temperatures above 600 °C. This phase transition was further studied using high-temperature X-ray diffraction techniques and the JMAK equation. The measurements revealed a dominating one-dimensional growth mechanism for $CsGaSe_2$-*mC*16 and a two-dimensional growth mechanism for $CsGaSe_2$-*mC*64. Furthermore, the effective activation energy of the phase transition was calculated using the obtained rate constants, and the effect of different grain sizes was investigated to some degree. The

DOI: 10.1021/acs.cgd.6b00532
Cryst. Growth Des. 2016, 16, 3983−3992

polymorphs were further studied by Raman and UV/vis spectroscopy.

EXPERIMENTAL SECTION

Synthesis of the Starting Materials. Gallium selenide GaSe was synthesized by chemical transport reaction from gallium (Chempur 99.99%) and selenium (Chempur 99.999%) using iodine (Sigma-Aldrich 99.8%) as transporting agent. Pure CsN_3 was obtained by passing hydrazoic acid (prepared by acidifying an aqueous solution of NaN_3 (Sigma-Aldrich 99.0%) into an aqueous solution of Cs_2CO_3 (Rockwood Lithium 99.9%). **Attention:** Condensed HN_3 is highly explosive. Tools made from transition metals must be avoided.

Synthesis of $CsGaSe_2$. The title compounds were synthesized by controlled thermal decomposition of CsN_3 combined with a stoichiometric mixture of GaSe and selenium in a quartz glass ampule under dynamic vacuum conditions. A flame-sealed ampule containing the raw product was annealed at elevated temperatures to yield $CsGaSe_2$. To obtain phase pure colorless $CsGaSe_2$-*mC*64, the samples were annealed at 580 °C. Phase pure yellow $CsGaSe_2$-*mC*16 was obtained by annealing above 600 °C and quenching of the ampule in water.

Single-Crystal X-ray Diffraction. Data collections on suitable single-crystals were performed on an Agilent Supernova at −150 °C using monochromatized Mo Kα radiation (λ = 0.71073 Å). The obtained diffraction data were corrected for Lorentz and polarization effects and corrected by an analytical absorption correction using the CrysAlisPro software package.[14] The resulting data sets had a completeness of 99.9% within 50° 2θ for both compounds. The crystal structure was solved by charge flipping methods using SUPERFLIP[10] (implemented in Jana2006[11]) and refined on F^2 with Jana2006[11] using full-matrix least-squares methods. The experimental parameters and details of the structure solution and refinement are summarized in Table 1.

X-ray Powder Diffraction. The X-ray powder diffraction experiments were performed on a STOE STADI P diffractometer equipped with a Dectris Mythen 1K detector and a high-temperature capillary furnace. Monochromatized Mo Kα1 radiation (λ = 0.70930 Å) was used in all experiments. The air sensitive samples were flame-sealed in a 0.3 mm quartz glass capillary and placed in another 0.5 mm quartz glass capillary due to the furnace architecture. To ensure reproducible results, all fine powdered samples were sieved using analytical sieves (Retsch GmbH) prior to the experiments (fraction 0.02−0.04 mm grain size). The $WinX^{POW}$ software package from STOE & Cie[20] was used for data collection and processing. The furnace temperature was controlled with a Eurotherm 24.16 controller (ΔT = ±1 °C). Corundum powder was used in the form of NIST Standard Reference Material 676.

Differential Thermal Analysis. Differential thermal analysis of the compound was performed on a SETARAM TG-DTA 92 16.18 in an evacuated quartz glass ampule using Al_2O_3 as reference material. The measurements were performed in the range 25−800 °C with a heating and cooling rate of 10 °C/min.

Vibrational Spectroscopy. The Raman spectra were recorded on a DXR SmartRaman Spectrometer from Thermoscientific (Excitation wavelength λ = 780 nm) in the range 150−1000 cm^{-1} with a resolution of 0.5 cm^{-1}.

UV/Vis Spectroscopy. Diffuse reflectance measurements were performed with a Bruins Omega 20 UV/vis spectrometer using $BaSO_4$ as a reference (100% reflectance). The absorption data was calculated using a modified Kubelka−Munk function.[28]

ASSOCIATED CONTENT

Supporting Information

The Supporting Information is available free of charge on the ACS Publications website at DOI: 10.1021/acs.cgd.6b00532.

Lists of anisotropic displacement parameters (Table S1, S2), interatomic distances (Table S3, S4), and plots of $t/t_{0.5}$ against α for all transitions (Figure S1, S2, S3) (PDF)

Accession Codes

CCDC 1474649−1474650 contain the supplementary crystallographic data for this paper. These data can be obtained free of charge via www.ccdc.cam.ac.uk/data_request/cif, or by emailing data_request@ccdc.cam.ac.uk, or by contacting The Cambridge Crystallographic Data Centre, 12 Union Road, Cambridge CB2 1EZ, UK; fax: +44 1223 336033.

AUTHOR INFORMATION

Corresponding Author

*E-mail: arno.pfitzner@chemie.uni-regensburg.de.

Notes

The authors declare no competing financial interest.

ACKNOWLEDGMENTS

The authors would like to thank Prof. Dr. Wolfgang Bensch (University of Kiel) for helpful comments regarding the crystallization kinetics and Prof. Dr. Manfred Scheer (University of Regensburg) for the Raman measurements. We would further like to thank Constantin Pompe (University of Regensburg) for helpful discussions regarding the Rietveld refinement using a fundamental parameter approach and Rockwood-Lithium GmbH for supplying cesium carbonate.

REFERENCES

(1) Krebs, B. *Angew. Chem.* **1983**, *95*, 113−134.
(2) Zondy, J.-J.; Bielsa, F.; Douillet, A.; Hilico, L.; Acef, O.; Petrov, V.; Yelisseyev, A.; Isaenko, L.; Krinitsin, P. *Opt. Lett.* **2007**, *32*, 1722−1724.
(3) Petrov, V.; Yelisseyev, A.; Isaenko, L.; Lobanov, S.; Titov, A.; Zondy, J.-J. *Appl. Phys. B: Lasers Opt.* **2004**, *78*, 543−546.
(4) Deiseroth, H. J. *Z. Kristallogr. - Cryst. Mater.* **1984**, *166*, 283−295.
(5) Friedrich, D.; Schlosser, M.; Pfitzner, A. *Z. Anorg. Allg. Chem.* **2014**, *640*, 826−829.
(6) Do, J.; Kanatzidis, M. G. *Z. Anorg. Allg. Chem.* **2003**, *629*, 621−624.
(7) Deiseroth, H. J.; Han, F. S. *Stud. Inorg. Chem.* **1983**, *3*, 655−658.
(8) Friedrich, D.; Schlosser, M.; Pfitzner, A. *Z. Anorg. Allg. Chem.* **2014**, *640*, 2356.
(9) Avrami. *J. Chem. Phys.* **1939**, *7*, 1103−1112. Avrami, M. *J. Chem. Phys.* **1940**, *8*, 212−224. Avrami, M. *J. Chem. Phys.* **1941**, *9*, 177−184.
(10) Palatinus, L.; Chapuis, G. *J. Appl. Crystallogr.* **2007**, *40*, 786−790.
(11) Petricek, V.; Dusek, M.; Palatinus, L. *Z. Kristallogr. - Cryst. Mater.* **2014**, *229*, 345−352.
(12) Spek, A. L. *Acta Crystallogr., Sect. D: Biol. Crystallogr.* **2009**, *65*, 148−155.
(13) Müller, D.; Poltmann, F. E.; Hahn, H. *Z. Naturforsch., B: J. Chem. Sci.* **1974**, *29B*, 117−118.
(14) *CrysAlisPro*, Version 1.171.38.37b; Rigaku Oxford Diffraction: 2015.
(15) Friedrich, D.; Pielnhofer, F.; Schlosser, M.; Weihrich, R.; Pfitzner, A. *Chem. - Eur. J.* **2015**, *21*, 1811−1817.
(16) Winkler, V.; Schlosser, M.; Pfitzner, A. *Z. Anorg. Allg. Chem.* **2015**, *641*, 549−556.
(17) Ward, M. D.; Pozzi, E. A.; Van Duyne, R. P.; Ibers, J. A. *J. Solid State Chem.* **2014**, *212*, 191−196.
(18) Shannon, R. D. *Acta Crystallogr., Sect. A: Cryst. Phys., Diffr., Theor. Gen. Crystallogr.* **1976**, *32*, 751−767.
(19) Boon, J. W.; MacGillary, C. H. *Recueil Trav. Chim. Pays-Bas.* **1942**, *61*, 910−920.
(20) *WinX^{POW}*, Version 3; Stoe & Cie GmbH: Darmstadt, 2014.
(21) Sharp, J. H.; Brindley, G. W.; Achar, N. N. *J. Am. Ceram. Soc.* **1966**, *49*, 379−382.
(22) Engelke, L.; Schaefer, M.; Schur, M.; Bensch, W. *Chem. Mater.* **2001**, *13*, 1383−1390.

DOI: 10.1021/acs.cgd.6b00532
Cryst. Growth Des. 2016, 16, 3983−3992

(23) Kiebach, R.; Schaefer, M.; Porsch, F.; Bensch, W. *Z. Anorg. Allg. Chem.* **2005**, *631*, 369−374.
(24) Zhou, Y.; Antonova, E.; Bensch, W.; Patzke, G. R. *Nanoscale* **2010**, *2*, 2412−2417.
(25) Hancock, J. D.; Sharp, J. H. *J. Am. Ceram. Soc.* **1972**, *55*, 74−77.
(26) Hulbert, S. F. *J. Br. Ceram. Soc.* **1969**, *6*, 11−20.
(27) Kempen, A. T. W.; Sommer, F.; Mittemeijer, E. J. *J. Mater. Sci.* **2002**, *37*, 1321−1332.
(28) Kisch, H. *Angew. Chem., Int. Ed.* **2013**, *52*, 812−847.
(29) Benmakhlouf, A.; Bentabet, A.; Bouhemadou, A.; Maabed, S.; Khenata, R.; Bin-Omran, S. *Solid State Sci.* **2015**, *48*, 72−81.
(30) Weihrich, R. *Private Communication* **2016**.

DOI: 10.1021/acs.cgd.6b00532
Cryst. Growth Des. 2016, 16, 3983−3992